Published in final edited form as:
Adv Funct Mater. 2023 December 22; 33(52): . doi:10.1002/adfm.202306117.

A highly sensitive and long-term stable wearable patch for continuous analysis of biomarkers in sweat

Farnaz Lorestani[a], **Xianzhe Zhang**[a], **Abu Musa Abdullah**[a], **Xin Xin**[a], **Yushen Liu, MD**[a], **Mashfiqur Rahman**[a], **Md Abu Sayeed Biswas**[a], **Bowen Li**[a], **Ankan Dutta**[a,b], **Zhenyuan Niu**[a], **Shuvendu Das**[a], **Shishir Barai**[a], **Ke Wang**[c], **Huanyu Cheng**[a]

[a]Department of Engineering Science and Mechanics, Pennsylvania State University, University Park, PA,16802, USA

[b]Center for Neural Engineering, The Pennsylvania State University, University Park, PA, 16802, USA

[c]Materials Research Institute, The Pennsylvania State University, University Park, PA 16802

Abstract

Although increasing efforts have been devoted to the development of non-invasive wearable or stretchable electrochemical sweat sensors for monitoring physiological and metabolic information, most of them still suffer from poor stability and specificity over time and fluctuating temperatures. This study reports the design and fabrication of a long-term stable and highly sensitive flexible electrochemical sensor based on nanocomposite-modified porous graphene by simple and facile laser treatment for detecting biomarkers such as glucose in sweat. The laser-reduced and patterned stable conductive nanocomposite on the porous graphene electrode provides the resulting glucose sensor with an excellent sensitivity of 1317.69 $\mu AmM^{-1}cm^{-2}$ with an ultra-low limit of detection (LOD) of 0.079 µM. The sensor can also detect pH and exhibit extraordinary stability to maintain more than 91% sensitivity over 21 days in ambient conditions. Taken together with a temperature sensor based on the same material system, the dual glucose and pH sensor integrated with a flexible microfluidic sweat sampling network further results in accurate continuous on-body glucose detection calibrated by the simultaneously measured pH and temperature. The low-cost, highly sensitive, and long-term stable platform could facilitate and pave the way for the early identification and continuous monitoring of different biomarkers for non-invasive disease diagnosis and treatment evaluation.

Graphical Abstract

This study reports the design and fabrication of a long-term stable and highly sensitive flexible electrochemical sensor based on nanocomposite-modified porous graphene by simple and facile laser treatment for detecting biomarkers such as sweat glucose with an excellent sensitivity and an ultra-low limit of detection (LOD).

---

fkl5072@psu.edu (F.L.) and huanyu.cheng@psu.edu (H.C.).

Keywords

flexible electrochemical biosensors; long-term stability; porous graphene nanocomposite electrode; laser treatment and patterning; accurate glucose sensing calibrated by pH and temperature

1. Introduction

Wearable and flexible electrochemical biosensors have attracted substantial interest because they enable accurate and noninvasive detection of biomarkers.[1–5] Compared with biofluids like tears, saliva, and urine, sweat is ideal for continuous and noninvasive biomarker detection due to its convenient on-body sampling possibility to rapidly reflect the physical body condition.[6–9] Despite the great potential, sweat-sensing devices still face challenges in real-time sweat sampling and need a highly sensitive, selective, and long-term stable sensing platform. Besides, the biosensor read-out is often affected by variations in the sweat pH, salinity, temperature, and other physiochemical factors. Furthermore, human sweat with a varied salinity (10–100 mM) and pH (4.5–7) is subject to temperature variation associated with exercise and ambient conditions, which can impact the measurement of biomarkers.[10–14] The temperature can also greatly affect the activity of enzymes in enzymatic sensors.[15] Therefore, integrating flexible physiological sensors to detect pH and temperature in a non-invasive sweat biosensing platform can calibrate the biomarker measurement for improved readout accuracy. Also, low-cost sensors applied over a large population are needed to account for individual differences in personalized medicine and population health. Furthermore, temperature changes associated with exercise and possible high ambient temperature conditions can greatly affect the activity of enzymes and ensure the accuracy of targeted biomarkers concentration readings.[15] Consequently, the integration of flexible physiological sensing platforms with wearable biological sensors for an accurate result is a must. On the other hand, sweat biosensors often need to work close to their limit of detection because the concentration of biomarkers in sweat is generally lower than that in interstitial fluids or blood.[16–18] The sweat biomarkers typically exhibit low concentration levels compared with their counterparts in blood and can vary depending on factors such as individual differences, hydration status, physical activity, and overall health. On average, the sweat glucose concentration ranges from ca. 0.2 to 2.0 millimoles per liter (mmol/L) or approximately 3.6 to 36 milligrams per deciliter (mg/dL).[19,20] In summary, it is challenging to develop a highly sensitive, selective, low-cost, and long-term stable flexible sensing platform for continuous and accurate healthcare monitoring.

With a simple fabrication process, laser-induced graphene (LIG) electrodes as an affordable, flexible, and multifunctional candidate start to gain momentum for electrochemical biosensors and electrical platforms.[21–25] However, low sensitivity and limited surface area can limit the detection of ultra-low biomarker concentration in sweat or other fluids. As a result, a wide range of conductive nanomaterials has been incorporated into the porous structure of LIG to increase the available surface area, facilitate electron transfer, and enhance the electrocatalytic activity of the electrode.[26–28] For instance, two-dimensional (2D) carbon materials such as graphene and reduced graphene oxide (rGO) can facilitate electron transfer for enhanced catalytic activities on the electrode.[29–31] Despite a high edge density on the 2D sheets, it is greatly reduced in the 3D arrangement. On the other hand, 1D carbon nanotubes (CNTs) with extraordinary conductivity, high aspect ratio, and chemical and mechanical stability can provide highly available 3D surface area and facilitate catalytic electron transferring, but their surface charge density is lower than GO.[32,33] Although the unique interactions between matrix and nanoparticles provide a range of property combinations to engineer properties of the biosensing platforms, the design and development remain heuristic and challenging. Hence, it would be of high interest to systematically design and optimize the performance of the rGO–CNT composite for maximized edge density in 3D arrangements.

This work reports a long-term stable, flexible sensing platform based on laser-reduced and patterned porous graphene nanocomposites for highly sensitive, selective, and accurate monitoring of biomarkers. With the facile laser treatment that is used to pattern the porous LIG electrode, a 3D network of highly conductive noble metal alloys and carbon-based nanocomposite materials is easily created on the LIG electrode. Besides the increased sensitivity, the LIG nanocomposites also exhibit significantly higher stability compared with the drop-casting of pre-synthesized nanomaterials that also need to use complicated and multistep processes (e.g., chemical, thermal, and electrochemical reduction processes). The laser-reduced and patterned LIG nanocomposite electrode provides a highly stable and sensitive platform for dual non-enzymatic glucose and pH measurements. Combined with a flexible LIG-based temperature sensor, the wearable device can calibrate glucose detection based on simultaneously measured temperature and pH. Integrated with a microfluidic network for sweat sampling, the wearable device demonstrates a high potential to conveniently, accurately, and continuously analyze sweat in diverse conditions for practical use. The low-cost integrated sensing platform can also be facilely adapted to measure other health-relevant biomarkers such as metabolites, hormones, neuropeptides, and cytokines from various biofluids for individual and population health, personalized medicine, and precision nutrition.

2. Results and discussion

2.1. Device Structure

The wearable microfluidic sensing device includes three major components: an electrochemical dual glucose and pH sensor, a temperature sensor, and a stretchable microfluidic network for sweat sampling (Figure 1A). The hydrophilicity-enhanced polyethylene glycol-polydimethylsiloxane (PEG-PDMS)[34,35] is used to fabricate the stretchable microfluidic layers with coil-shaped microfluidic channels and inlet/outlet wells for self-driven on-body sweat uptake (Figure 1B; see the design and fabrication procedure in Figures S1–S2, Supporting Information). The dual glucose/pH and temperature sensors are aligned and bounded with coil-shaped microfluidic channels from the top and bottom after plasma treatment. The electrochemical dual glucose and pH sensor exploits three LIG-based electrodes with the working electrode (WE) modified with laser-reduced nanocomposite for enhanced sensitivity and stability (Figure 1C). The wearable patch can be comfortably mounted on different locations of the human body such as arms with a skin-adhesive layer for sweat sampling and analysis (Figure 1D).

2.2. Design and characterization of flexible dual glucose/pH sensor

2.2.1. Nanocomposite modification—The design of the high-performance flexible dual glucose and pH sensor consisting of three LIG electrodes (Figure 2A) relies on engineered modification of the working electrode with conductive material and nanocomposite to facilitate the electrocatalytic performance for electrochemical glucose detection (Figure 2B). When glucose comes into contact with the metal-modified electrode, it undergoes oxidation at a lower potential compared to traditional carbon-based electrodes. This oxidation generates a measurable current or potential change, which is directly proportional to the glucose concentration in the solution. The metal catalyst enhances the electrochemical activity and selectivity towards glucose oxidation, enabling accurate and rapid glucose sensing.[36–38] The LIG electrode is modified by the GO–CNT composite to effectually combine the high 3D surface area of CNT with the high charge density of GO for dramatically increased edge density per unit nominal area with an excellent catalytic effect for electrochemical detection. The hydrophilic oxygen groups and multiple aromatic parts in GO could also assist in obtaining a stable GO-CNT complex with a strong π–π stacking interaction. Considering the catalytic activity of various metals and their alloys,[39–44] the LIG electrode modified by the carbon-base nanomaterials is further decorated with metal nanoparticles followed by laser treatment for enhanced electrochemical properties.

An easy and tunable deposition way for small and flexible electrodes is drop-casting, the nanomaterial with different volume ratios can easily be dispersed by ultrasonication force into the desired solvent and spread over the electrode area followed by drying under controlled conditions. The modified nanomaterial LIG sensor fabrication is shown in the first three steps in Supplementary (Figure S2A, Supporting Information), the catalyst activity is evaluated with cyclic voltammetry (CVs) to detect 1 mM glucose in a 0.1M NaOH solution. The sensor with the LIG/rGO-CNT nanocomposite exhibits higher sensitivity toward glucose detection (Figure 2C) compared to that with the LIG/CNT or LIG/rGO electrode.[45,46] Further, introducing gold nanoparticles (AuNPs) into the nanocomposite significantly increases glucose oxidation cathodic peaks as the gold-to-carbon-based matrix ratio increases from 1:1 to 1:6 possibly due to reduced agglomeration of gold particles in the high matrix ratio (Figure 2D). The existence of silver nanorods (AgNRs) in the Ag/AuNPs–rGO-CNT nanocomposite can also enhance the catalytic activity toward glucose detection.

The AgNRs/AuNPs–rGO-CNT with a volume ratio of 1:1:6 shows an increase in the oxidation peak for glucose detection due to the synergistic contribution of the alloy's components in the synthesized composite for increased electrochemical activity (Figure 2E). The ratio 1:1:12 of the AgNRs/AuNPs–rGO-CNT nanocomposite indicates a well-defined glucose oxidation peak possibly due to the increased available surface area as a result of less agglomeration of silver nanorods and gold nanoparticles in the nanocomposite (Figure 2E).[47–49] The AgNRs/AuNPs–rGO-CNT nanocomposite sensor exhibits higher sensitivity toward glucose detection (Figure 2F) compared to carbon-based and silver or gold carbon nanocomposites-modified electrodes.

The effect of the drop-casted nanomaterial on the sensor performance is further characterized by Field Emission Scanning Electron Microscopy (FESEM) (Figure S3, Supporting Information). Despite being simple and accessible, drop-casting that depends on solvent properties and the solvent evaporation rate is often associated with nanomaterial agglomeration, concentration gradient, and non-uniform coating due to different evaporation rates across the electrode surface and fast in-plane diffusion.[50] Indeed, the agglomeration of the metal nanoparticles in the carbon matrix is not negligible (Figure S3b(i), Supporting Information). The characterized electrochemical activity of the resulting sensors towards glucose detection also exhibits low repeatability and stability despite applying common physical modification methods such as tuning the nanomaterial component volume ratio,[51] solvent hydrophilicity,[52] and optimizing solvent evaporation rate or annealing (50°C for 5 min).[53] Also, the synthesized Ag/AuNPs-rGO-CNT nanocomposite was further characterized by Transmission Electron Microscopy (TEM) image and corresponding elemental mapping analysis. The result confirms the agglomeration of the metals in the carbon matrix nanocomposite (Figure S5, Supporting Information).

2.2.2. Characterization of laser treatment—To address the issues of nanomaterial agglomeration and improve the stability and repeatability of the modified film on the electrode in the sensor,[54–56] laser scribing is exploited to help create LIG nanocomposite-based electrodes. Inspired by the approach that uses a laser to reduce GO to rGO electrodes with notable stability under high mechanical stress,[57,58] we introduce the direct laser treatment on the LIG nanocomposite for uniform and repeatable nanomaterial deposition. After drop-casting of the optimized ratio of the synthesized AgNRs/AuNPs–GO-CNT nanocomposite material on the LIG WE followed by drying in ambient conditions, the laser treatment is performed using 10.5% of maximum power, 11% of maximum speed, 1000 PPI, and an image density 6 (Figure 3A). The controlled high-power CO_2 laser also reduces GO into conductive, crack-free, and robust rGO,[57,59,60] which avoids damaging the substrate that often occurs in chemical,[61] thermal,[54] and electrochemical[62] reduction methods. The FTIR spectrum of GO-CNT and Ag/AuNPs-GO-CNT films before and after laser treatment indicates that the broad peak from O–H stretching vibrations at 3265 cm^{-1} disappears after the laser treatment. The peaks at 1729, 1624, 1366, and 1057 cm^{-1} are attributed to C=O stretching, C=C aromatic ring stretching bond and O–H bending, C–OH stretching, and C–O–C stretching, respectively. The broad peaks at 3318 and 3844 cm^{-1} could be ascribed to absorbed water molecules O–H stretching vibrations (Figure 3B).[63]

Noble metal nanocrystals with superior electrocatalytic performance such as bimetallic Ag-Au can be controllably synthesized with laser treatment of AgNRs and AuNPs. The AgNRs under laser treatment are initially transformed into shorter nanorods and then into NPs.[64] The effect of laser treatment on the nanocomposite is further investigated by the TEM, SEM, and elemental mapping EDS characterizations. As we discussed before, the TEM images and corresponding elemental mapping analysis of the AgNRs/AuNPs-GO-CNT nanocomposite before laser treatment indicate that the metals are not well dispersed in the carbon matrix and mainly agglomerated on the edges of graphene oxide sheets and wrinkles (Figures 3C–E and Figure S5, Supporting Information). In comparison, the FESEM images and corresponding elemental mapping of the nanocomposite on the LIG WE after laser treatment confirm the obvious change from an agglomeration of AgNRs and AuNPs on wrinkled GO-CNT to well-dispersed decorations of Ag/Au nanoparticles on an overlapped 3D network structure of rGO-CNT flakes (Figures 3F–H, and Figure S6, Supporting Information). The dispersion of the components in the laser-treated nanocomposite is further confirmed by the EDS analysis (Figure S4, Supporting Information). Because the surface morphology and chemistry significantly impact the active surface area, electrical conductivity, and electrocatalyst activity,[65,66] the electrode based on the resulting LIG nanocomposite can provide long-term stable electrochemical sensing. The XPS analysis further investigates the valence state of the chemical bonding of the Ag/AuNPs-rGO-CNT nanocomposite before and after laser treatment (Figure 4). The survey scan spectrum of the Ag/AuNPs-rGO-CNT nanocomposite after laser treatment confirms the presence of predominant peaks at 370, 350, 590, and 85 eV binding energies, corresponding to the Ag 3d, Au 4d, Ag 3p, and Au 4f, respectively (Figure 4A). The primary shape at 284 eV is consistent with a sp2 graphitic carbon peak of the Ag/AuNPs-rGO-CNT nanocomposite before (Figure 4Bi), and after (Figure 4Ci) laser treatment, but a high energy side of the trailing edge of the main peak that suggests that a C-O or C=O component is less visible after laser treatment (Figure 4Ci). In the high-resolution spectrum of the Au 4f region, the binding energies at 84.05 and 87.72 eV are attributed to Au 4f7/2 and Au 4f5/2 of the metallic Au, ensuring the zero-oxidation state of the AuNPs deposited in the carbon-based nanocomposite matrix before (Figure 4Bii), and after (Figure 4Cii) laser treatment. The high-resolution spectrum of the Ag 3d region of laser-treated Ag/AuNPs-rGO-CNT nanocomposite also shows a higher intensity in the peaks at 368.26 and 374.26 eV corresponding to 3d5/2 and 3d3/2 (Figure 4Ciii) than that before laser treatment (Figure 4Biii), which also confirms higher existence of Ag in the zero valence state after laser treatment. Also, the intensity of the Ag oxide peaks at 368.82 and 374.82 eV correspond to Ag (oxide) 3d5/2 and 3d3/2 in the nanocomposite is much lower after laser treatment.

2.2.3. Characterization of biosensor performance—Evaluation of the laser-treated Ag/AuNPs-rGO-CNT nanocomposite-modified LIG electrodes for non-enzymatic glucose detection reveals the improved electrochemical performance due to an increased available surface area and higher conductivity (Figure 5A). By applying a small voltage to the sensor, the measured faradaic current generated from the non-enzymatic oxidation of glucose is calibrated for the detection of glucose concentration. Different potentials applied by chronoamperometry to oxidize the glucose of a specific concentration determine the optimized value of 0.7 V (Figure S8, Supporting Information) to achieve a high sensitivity of 1317.69 $\mu AmM^{-1}cm^{-2}$ (higher than that of 312.55 $\mu AmM^{-1}cm^{-2}$ without laser treatment) and low limit of detection (LOD) of 0.079 μM (Figure 5B, and C).

The improved performance is likely attributed to the high specific surface area to facilitate electron and ion transfer for electrocatalyst activities. Generally, metal nanoparticles (NPs) such as Ag and Au NPs have a negative surface charge as a consequence of their negative ζ-potential values.[67] As a result, the modified Ag/AuNPs-rGO-CNT alloy nanocomposite glucose sensor provides good selectivity by repelling negatively charged analytes such as UA and AA, with a selectivity factor of 0.6039 following the calculation in the literature.[68] Also, the optimized low applied voltage reduces the oxidation of other analytes to give enhanced selectivity towards glucose. In addition to the good selectivity (Figure 5D), the non-enzymatic sensor also exhibits excellent stability even for storage at room temperature in the ambient (or ionic solution) condition between the measurements over three weeks (Figure 5E and Figure S9, Supporting Information). Compared with a sensitivity loss of more than 20% from the Ag/AuNPs-rGO-CNT alloy nanocomposite glucose sensor without laser treatment, the laser-treated sensor only shows a sensitivity loss of less than 9% over three weeks (Figure 5F). The significantly improved stability from laser treatment is likely attributed to the high-temperature annealing as previously reported.[69] Meanwhile, the sensitivity of the glucose sensor can be further increased when operated at elevated temperatures such as those relevant to heat stress (Figure 5G). Taken together with the high linearity, a fast response time of under 5 s, and excellent stability, the obtained glucose sensor compares favorably with the previous literature reports(Table S4, Supporting Information).

2.2.4. Characterization of the dual-mode sensor for pH sensing—Because rGO as a protonated probe responds to pH,[70] the laser-treated Ag/AuNPs-rGO-CNT nanocomposite-modified LIG electrode can serve as a dual-mode sensor to detect pH variations. Cyclic voltammetry with a scan rate of 1 mV/s is selected to evaluate the electrochemical redox activity and detect the pH (Figure S10, Supporting Information), as the background capacitance shows a large influence at a higher scan rate. The measured cyclic voltammetry in different pH buffer solutions shows the anodic peak potentials during the anodic reaction associated with hydroquinone oxidation and the cathodic peak potential from the quinone/hydroquinone redox couple (Figure S10a, Supporting Information), which is consistent with the literature report.[71] The obtained anodic potential exhibits a highly linear dependence on the pH in the physiologically relevant range from 4 to 8, with a sensitivity of 0.3565 $\mathrm{VpH^{-1}cm^{-2}}$ (Figure 5H). The use of CV for pH measurement based on peak potential is different from CA measurements for glucose to give different units in the obtained sensitivity. Besides enhanced accuracy and sensitivity, these measurements also allow for direct comparison with the previously reported literature for each target analyte.

2.3. Design and characterization of flexible LIG-based temperature sensor

Despite the increased sensitivity of the glucose sensor at elevated temperatures, the fluctuations in the temperature during glucose detection could lead to inaccurate readings. Therefore, it is of high importance to integrate temperature sensors to calibrate the temperature effect.[72,73] By exploiting a serpentine-shaped pattern, the LIG temperature sensor is designed to encompass the dual-mode electrochemical sensor to sensitively detect the temperature change in the region (Figure S11, Supporting Information). The linear fit between the measured relative resistance changes and the temperature in the physiologically relevant range from 22 to 58°C gives a sensitivity of −3.937 Ohm/°C (Figure 5I).

2.4. Calibration of the glucose sensor with simultaneously measured pH and temperatures

The fast response time of the glucose sensor in the range of 3–5 s allows rapid *in vitro* characterization of its linear response curves from 10 μM to 5 mM at various pH levels and temperatures. The calibration of the glucose sensor based on the simultaneously measured temperature and pH starts with the determination of the glucose sensor responses as a function of the temperature and pH (Figures 6A, and B). The amperometric current signal to a given glucose concentration increases with the increasing temperature and pH. Next, the correction factors in the linear fit between the amperometric current and glucose concentration as a function of body temperature and sweat pH are determined from these calibration curves (Figures 6C, and D). The calibrated glucose concentration is then obtained with the corrected slope and intercept in the linear fit (see details in Supporting Information 1.6.1).

2.5. On-body evaluation of the calibrated glucose sensor integrated with a microfluidic patch.

The integration of the calibrated glucose sensor with a microfluidic device provides a means for on-body sweat sampling and glucose analysis. Evaluation of the sensor performance in near-neutral solutions such as artificial sweat that closely mimics the chemical compositions of human perspiration could ensure safety and reliability for on-body measurements. The laser-treated Ag/AuNPs-rGO-CNT nanocomposite-modified sensor is first calibrated in the artificial sweat with various glucose concentrations before the on-body measurement (Figure S12, Supporting Information). The accuracy of the sweat glucose concentration measured by the laser-treated nanocomposite sweat sensors right after, one hour after, and two hours after the meal is validated by the commercial glucometer that measures the blood glucose concentrations (Figure S14, Supporting Information).

With the help of a skin adhesive medical tape, the flexible integrated microfluidic patch can be robustly mounted on the skin even upon mechanical bending (Figure S13, Supporting Information). The patch on the forearm (Figures 6E, and F) can continuously collect sweat samples from the sweat glands under the inlet of the microfluidic device to dynamically analyze the glucose concentration before, immediately after, and 1 h after the meal (Figure 6G). As the sweat pH and body temperature fluctuate with human activities such as intensive exercise and body enzyme activity after eating, the sweat pH and the skin temperature are simultaneously measured (Figure 6G). As a result, the glucose measurements can be calibrated by using the corrected slope and intercept in the linear fit based on the measured temperature and pH for obtaining the accurate on-body glucose concentration (Figure 6I). The increased glucose concentration after a meal[74,75] is more accurately captured by real-time calibration based on the pH and temperature measurement.

3. Conclusion

In summary, this work presents the design and demonstration of a long-term stable wearable electrochemical sensing device based on laser-treated LIG nanomaterials. Besides the long-term stable response for at least 21 days, the resulting glucose sensor exhibits a remarkably high sensitivity of 1317.69 $\mu AmM^{-1}cm^{-2}$ in the range from 10 μM to 5 mM with an LOD of 0.079 μM. A more accurate glucose detection can be obtained by simultaneous measurements of sweat pH and skin temperature for calibration. The integration of the calibrated sensor with a flexible hydrophilic microfluidic device provides the noninvasive continuous on-body detection of glucose in sweat. The demonstrated highly stable and sensitive flexible sensing platform can pave the way for the development of next-generation sensors and devices for long-term non-invasive continuous monitoring of various biomarkers toward precision medicine and population health.

4. Experimental Methods

4.1. Chemicals and Materials

Ethanol (C_2H_5OH) was purchased from KOPTEC (King of Prussia, PA, USA), and N, N- Dimethylformamide (DMF) (HPLC grade, M=73.01 g/mol) was obtained from VWR, PA, USA. Gold (III) chloride hydrate ($HAuCl_4$), multi-walled carbon nanotube (>90% carbon, D×L= 110–170 nm × 5–9 μm), potassium phosphate monobasic (KH_2PO_4), potassium phosphate dibasic (K_2HPO_4), nitric acid (HNO_3, 98%), sulfuric acid (H_2SO_4, 98%), and potassium permanganate ($KMnO_4$, 99.9%) were purchased from Sigma-Aldrich, USA. Graphite flakes were procured from Asbury Inc, USA. Silver nanorods (D=50 nm, L=100–200 μm in water) obtained from ACS MATERIAL, LLC, USA. Commercial silver nanoparticle ink was purchased from NovaCentrix, USA. Polyimide (PI) tapes with a thickness of 50 μm were purchased from Dupont, USA. Deionized (DI) water (d= 1g/cm^3, M=18.02 g/mol) from Sigma-Aldrich, USA was used to prepare all kinds of solutions. Polydimethylsiloxane (PDMS; Sylgard 184) was purchased from the Dow Chemical Company, USA. Poly (ethylene glycol) (PEG) was purchased from Gelest Inc, PA, USA.

4.2. Preparation of nanocomposite and LIG non-enzymatic sensors

4.2.1. Synthesis of graphene oxide (GO)—Modified Hummers' method was applied to synthesize GO.[76] The GO solution (0.05 wt%) was dialyzed for 6h to remove additional acids or salts. Next, the unexfoliated GO was removed from the solution using a centrifuge at 3000 rpm (20 minutes). The suspension was further dried at 50°C for 24 hours.

4.2.2. Synthesis of silver nanorods-reduced graphene oxide-carbon nanotube nanocomposite (AgNRs–GO-CNT)—GO suspension was prepared by dispersing 5 mg of GO into 800 μL DI water and 200 μL ethanol, under sonication for 2 hours at room temperature. The same amount of CNT has been dispersed into a mixture of 600 μL DI water, 200 μL DMF, and 200 μL ethanol with sonication for 2 hours at room temperature. GO and CNT stock solutions were mixed with a volume ratio of 1:1 v/v. Next, the solution was stirred using a magnetic stirrer (RPM=330, 80°C) for 30 minutes. The GO-CNT dispersion and AgNRs dispersion were mixed with ratios of (1:1 v/v), (3:1 v/v), and (6:1 v/v) and sonicated for 2 hours to reach assimilation. The prepared AgNRs-GO-CNT mixture and chitosan solution (0.5 wt.%) were mixed with a volume ratio of 1:1 and sonicated for another 2 hours.

4.2.3. Synthesis of silver/gold alloy nanoparticle-reduced graphene oxide-carbon nanotube nanocomposite (AgNRs/AuNPs-GO-CNT)—The stock dispersion of GO-CNT in water 1:1 v/v, AgNRs dispersion, and 0.1 mol $HAuCl_4$ solution were mixed with a volume ratio of 6:1:1 and 12:1:1. Next, the solution was stirred using a magnetic stirrer (RPM=330, 80°C) for 30 minutes. The prepared AgNRs/AuNPs-GO-CNT mixture and chitosan solution (0.5 wt.%) were mixed with a volume ratio of 1:1 and stirred again for another 30 minutes.

4.2.4. Fabrication of laser-induced graphene (LIG) electrode—After rinsing and cleaning the PI film with ethanol and distilled (DI) water followed by drying in the air, it was mounted to a glass slide for laser scribing. A 30W CO_2 laser (VLS2.30, Universal Laser Systems, Inc. VLS2.3) with raster mode was used to create the design of three LIG electrodes with the following optimized settings: 10.5 % of maximum power, 11 % of maximum speed, 1000 PPI, and image density of 6.

4.2.5. Fabrication of LIG-based reference electrode (RE)—The prepared LIG electrode was coated with a commercial silver nanoparticle (AgNPs) ink (JS-A191, Novacentrix) to integrate Ag/AgCl for the reference electrode (RE). The solvent in the AgNPs ink was vaporized during photonic sintering of the ink using xenon light pulses, leaving conductive traces on the LIG surface. The resulting Ag/LIG electrode was soaked in the $FeCl_3$ solution for 1 minute, washed with DI water, and then allowed to dry completely in the air. Applying three drops of Nafion to the electrode completed the fabrication of the Nafion Ag/AgCl/ LIG RE.

4.2.6. Fabrication of LIG-based working electrode (WE) modified with the synthesized nanocomposite.—The working electrode (WE) was prepared by modifying the LIG electrode with the synthesized AgNRs/AuNPs-rGO-CNT nanocomposite by drop-casting 20 μL of the prepared solution on the LIG electrode and complete drying in ambient conditions.

4.2.7. Laser treatment of the nanocomposite-modified WE—Laser treatment was performed on the modified WE with AgNRs/AuNPs-rGO-CNT nanocomposite using 10.5% maximum power, 11 % maximum speed, 1000 PPI, and an image density of 6.

4.2.8. Fabrication of temperature sensor—The LIG-based temperature sensor with designed patterns was fabricated by the same method described in 4.2.4. section (For geometric parameters and dimensions of the temperature sensor please see Figure S1, Supporting Information).

4.2.9. Fabrication of microfluidic channels—The microfluidic channels consisted of a bottom channel layer and a top encapsulation layer with an outlet. The PEG-PDMS was prepared using a modified Gökaltun's method.[77] In brief, the PDMS in a 1:10 wt/wt ratio (curing agent: base) mixed with 2.5 wt% of PEG was first vacuumed in a petri dish to remove the bubbles and then cured in a hot oven at 70°C for 20 minutes. The cured PEG-PDMS was laser scripted with a 30 W CO_2 laser (VLS2.30, Universal Laser Systems, Inc. VLS2.3) using raster mode with 10.5% of the maximum power, 11% of the maximum speed, 1000 PPI, and an image density of 6 to create the microfluidic channels. The laser-engraved channels were rinsed with DI water to remove the residuals created during laser engraving. The cleaned microfluidic channels were plasma treated for 5 minutes with a plasma cleaner (PDC-32G, Harrick Plasma) to improve the hydrophilicity of the surface. The top PEG-PDMS encapsulation layer with an outlet was created following the same process for further use. (For geometric parameters and dimensions of the microfluidic channels please see Figure S1, Supporting Information).

4.2.10. Assembly of integrated microfluidic electrochemical sensors—

The fabricated microfluidic layers were plasma treated for 5 minutes with a plasma cleaner before the assembly. Next, the fabricated electrochemical sensor and temperature sensor were sandwiched between plasma-treated microfluidic layers. An adhesive layer on the bottom surface of the assembled device provided easy attachment to the human skin for on-body measurements (Figure S2, Supporting Information).

4.3. Material characterization

The laser-induced Ag/AuNPs-rGO-CNT electrode film was characterized by Raman Spectroscopy, Scanning Electron Microscopy (SEM), Transmission Electron Microscopy (TEM), X-ray photoelectron spectroscopy (XPS), and Fourier-transform infrared (FTIR) spectroscopy. The FTIR measurements on Machine Bruker V70 (Wavenumber: 4000cm^{-1} to 600cm^{-1}, Resolution: 6 s^{-1}) were used to study the chemical bonding and identify organic and inorganic materials on the modified nanocomposite films using infrared light. The EDS was carried out to study the elemental composition of the Ag/AuNPs-GO-CNT film before and after laser treatment. Energy Dispersive Spectroscopy (EDS) equipped with SEM was performed on Machine FESEM Apreo 5, (Voltage: 3 kV, beam current: 13 pA), The XPS experiments were performed using a Physical Electronics VersaProbe III instrument equipped with a monochromatic Al kα x-ray source (hν = 1,486.6 eV) and a concentric hemispherical analyzer.

Supplementary Material

Refer to Web version on PubMed Central for supplementary material.

Acknowledgments

H.C. acknowledges the support from the National Institutes of Health (Award Nos. R21EB030140, R21OH012220, and R33HL154215), the National Science Foundation (NSF) (Grant Nos. ECCS-1933072, 2222654, and 2309323), and Penn State University. A.D. would like to acknowledge National Institutes of Health grant (T32NS115667) and the Leighton Riess Graduate Fellowship at Penn State University. MD Mashfiqur Rahman and Md Abu Sayeed Biswas contributed equally to this work.

References:

[1]. Qiao Y, Qiao L, Chen Z, Liu B, Gao L, Zhang L, Chemosensors 2022, 10, 273.

[2]. Mohan AMV, Rajendran V, Mishra RK, Jayaraman M, TrAC Trends Anal. Chem. 2020, 131, 116024.

[3]. Xu J, Fang Y, Chen J, Biosensors 2021, 11, 245. [PubMed: 34436047]

[4]. Promphet N, Ummartyotin S, Ngeontae W, Puthongkham P, Rodthongkum N, Anal. Chim. Acta 2021, 1179, 338643. [PubMed: 34535258]

[5]. Yang Y, Gao W, Chem. Soc. Rev. 2019, 48, 1465. [PubMed: 29611861]

[6]. Heikenfeld J, Electroanalysis 2016, 28, 1242.

[7]. Liu C, Xu T, Wang D, Zhang X, Talanta 2020, 212, 120801. [PubMed: 32113563]

[8]. Bariya M, Nyein HYY, Javey A, Nat. Electron. 2018, 1, 160.

[9]. Yun SM, Kim M, Kwon YW, Kim H, Kim MJ, Park Y-G, Park J-U, Appl. Sci. 2021, 11, 1235.

[10]. Sonner Z, Wilder E, Heikenfeld J, Kasting G, Beyette F, Swaile D, Sherman F, Joyce J, Hagen J, Kelley-Loughnane N, Biomicrofluidics 2015, 9, 31301.

[11]. Hianik T, Ostatná V, Sonlajtnerova M, Grman I, Bioelectrochemistry 2007, 70, 127. [PubMed: 16725379]

[12]. Zafar H, Channa A, Jeoti V, Stojanović GM, Sensors 2022, 22, 638. [PubMed: 35062598]

[13]. Hendricks AJ, Vaughn AR, Clark AK, Yosipovitch G, Shi VY, J. Dermatol. Sci. 2018, 89, 105. [PubMed: 29169766]

[14]. Schmid-Wendtner M-H, Korting HC, Skin Pharmacol. Physiol. 2006, 19, 296. [PubMed: 16864974]

[15]. Mondal S, Zehra N, Choudhury A, Iyer PK, ACS Appl. Bio Mater. 2020, 4, 47.

[16]. Moyer J, Wilson D, Finkelshtein I, Wong B, Potts R, Diabetes Technol. Ther. 2012, 14, 398. [PubMed: 22376082]

[17]. Heikenfeld J, Jajack A, Feldman B, Granger SW, Gaitonde S, Begtrup G, Katchman BA, Accessing analytes in biofluids for peripheral biochemical monitoring, Vol. 37, 2019, pp. 407–419.

[18]. Sim D, Brothers MC, Slocik JM, Islam AE, Maruyama B, Grigsby CC, Naik RR, Kim SS, Adv. Sci. 2022, 9, 2104426.

[19]. Hong YJ, Lee H, Kim J, Lee M, Choi HJ, Hyeon T, Kim D, Adv. Funct. Mater. 2018, 28, 1805754.

[20]. Lin P-H, Sheu S-C, Chen C-W, Huang S-C, Li B-R, Talanta 2022, 241, 123187. [PubMed: 35030501]

[21]. Wan Z, Nguyen N-T, Gao Y, Li Q, Sustain. Mater. Technol. 2020, 25, e00205.

[22]. Le TD, Phan H, Kwon S, Park S, Jung Y, Min J, Chun BJ, Yoon H, Ko SH, Kim S, Adv. Funct. Mater. 2022, 32, 2205158.

[23]. Liu J, Ji H, Lv X, Zeng C, Li H, Li F, Qu B, Cui F, Zhou Q, Microchim. Acta 2022, 189, 1.

[24]. Thakur AK, Singh SP, Thamaraiselvan C, Kleinberg MN, Arnusch CJ, J. Memb. Sci. 2019, 591, 117322.

[25]. Zhang C, Chen H, Ding X, Lorestani F, Huang C, Zhang B, Zheng B, Wang J, Cheng H, Xu Y, Appl. Phys. Rev. 2022, 9, 11413.

[26]. Lin S, Feng W, Miao X, Zhang X, Chen S, Chen Y, Wang W, Zhang Y, Biosens. Bioelectron. 2018, 110, 89. [PubMed: 29602035]

[27]. Zhao J, Zheng C, Gao J, Gui J, Deng L, Wang Y, Xu R, Sensors Actuators B Chem. 2021, 347, 130653.

[28]. Zhu B, Yu L, Beikzadeh S, Zhang S, Zhang P, Wang L, Travas-Sejdic J, Electrochim. Acta 2021, 378, 138132.

[29]. Wang F, Wang K, Zheng B, Dong X, Mei X, Lv J, Duan W, Wang W, Mater. Technol. 2018, 33, 340.

[30]. Lan L, Le X, Dong H, Xie J, Ying Y, Ping J, Biosens. Bioelectron. 2020, 165, 112360. [PubMed: 32729493]

[31]. Balkourani G, Damartzis T, Brouzgou A, Tsiakaras P, Sensors 2022, 22, 355. [PubMed: 35009895]

[32]. Settu K, Lai YC, Liao CT, Carbon nanotube modified laser-induced graphene electrode for hydrogen peroxide sensing, Vol. 300, 2021.

[33]. Zhao J, Luo J, Zhou Z, Zheng C, Gui J, Gao J, Xu R, Sensors Actuators A Phys. 2021, 323, 112658.

[34]. Moser T, Celma C, Lebert A, Charrault E, Brooke R, Murphy PJ, Browne G, Young R, Higgs T, Evans D, ACS Appl. Mater. Interfaces 2016, 8, 974. [PubMed: 26698297]

[35]. Long HP, Lai CC, Chung C-K, Surf. Coatings Technol. 2017, 320, 315.

[36]. Ju H, Zhang X, Wang J, Ju H, Zhang X, Wang J, NanoBiosensing Princ. Dev. Appl. 2011, 171.

[37]. Qian Y, Wang Y, Wang L, Rev. Anal. Chem. 2022, 41, 189.

[38]. Brouzgou A, Tsiakaras P, Top. Catal. 2015, 58, 1311.

[39]. Nasraoui S, Al-Hamry A, Anurag A, Teixeira PR, Ameur S, Paterno LG, Ben Ali M, Kanoun O, In 2019 16th International Multi-Conference on Systems, Signals & Devices (SSD), IEEE, 2019, pp. 615–620.

[40]. Zhang Y, Li N, Xiang Y, Wang D, Zhang P, Wang Y, Lu S, Xu R, Zhao J, Carbon N. Y. 2020, 156, 506.

[41]. Yoon H, Nah J, Kim H, Ko S, Sharifuzzaman M, Barman SC, Xuan X, Kim J, Park JY, Sensors Actuators B Chem. 2020, 311, 127866.

[42]. Nasraoui S, Al-Hamry A, Teixeira PR, Ameur S, Paterno LG, Ben Ali M, Kanoun O, J. Electroanal. Chem. 2021, 880, 114893.

[43]. Asaduzzaman M, Zahed MA, Sharifuzzaman M, Reza MS, Hui X, Sharma S, Do Shin Y, Park JY, Biosens. Bioelectron. 2023, 219, 114846. [PubMed: 36327564]

[44]. Yi N, Cheng Z, Li H, Yang L, Zhu J, Zheng X, Chen Y, Liu Z, Zhu H, Cheng H, Mater. Today Phys. 2020, 100265.

[45]. Hyeong S, Park M, Kim S, Park S, Choi K, Im MJ, Kim ND, Kim T, Lee SH, Park J, Adv. Mater. Technol. 2022, 7, 2101105.

[46]. Dutta A, Sathiyan K, Sharon D, Borenstein A, FlatChem 2022, 33, 100378.

[47]. Waqas M, Lan J, Zhang X, Fan Y, Zhang P, Liu C, Jiang Z, Wang X, Zeng J, Chen W, Electroanalysis 2020, 32, 1226.

[48]. Hatamluyi B, Lorestani F, Es'haghi Z, Biosens. Bioelectron. 2018, 120.

[49]. Ghadimi H, Nasiri-Tabrizi B, Nia PM, Basirun WJ, Tehrani RMA, Lorestani F, RSC Adv. 2015, 5.

[50]. Yunus Y, Mahadzir NA, Mohamed Ansari MN, Tg Abd Aziz TH, Mohd Afdzaluddin A, Anwar H, Wang M, Ismail AG, Polymers (Basel). 2022, 14, 1112. [PubMed: 35335442]

[51]. Wang Q, Cui X, Chen J, Zheng X, Liu C, Xue T, Wang H, Jin Z, Qiao L, Zheng W, RSC Adv. 2012, 2, 6245.

[52]. Lorestani F, Nia PM, Alias Y, Manan NSA, J. Electrochem. Soc. 2015, 162.

[53]. Park J-M, Sohn I-B, Kang C, Kee C-S, Hwang I-W, Yoo HK, Lee JW, Opt. Commun. 2016, 359, 349.

[54]. Lorestani F, Shahnavaz Z, Mn P, Alias Y, Manan NSA, Sensors Actuators, B Chem. 2015, 208.

[55]. Zhang C, Peng Z, Huang C, Zhang B, Xing C, Chen H, Cheng H, Wang J, Tang S, Nano Energy 2021, 81, 105609.

[56]. Enaganti PK, Kothuru A, Goel S, J. Mater. Res. 2022, 1.

[57]. El-Kady MF, Strong V, Dubin S, Kaner RB, Science (80-.). 2012, 335, 1326.

[58]. Kumar R, Joanni E, Singh RK, da Silva ETSG, Savu R, Kubota LT, Moshkalev SA, J. Colloid Interface Sci. 2017, 507, 271. [PubMed: 28802194]

[59]. Viskadouros G, Konios D, Kymakis E, Stratakis E, Appl. Phys. Lett. 2014, 105, 203104.

[60]. Gao W, Singh N, Song L, Liu Z, Reddy ALM, Ci L, Vajtai R, Zhang Q, Wei B, Ajayan PM, Nat. Nanotechnol. 2011, 6, 496. [PubMed: 21804554]

[61]. Adeniyi O, Nwahara N, Mwanza D, Nyokong T, Mashazi P, Appl. Surf. Sci. 2023, 609, 155234.

[62]. Urhan BK, Demir Ü, Özer TÖ, Doğan HÖ, Thin Solid Films 2020, 693, 137695.

[63]. Cheng C, Nie S, Li S, Peng H, Yang H, Ma L, Sun S, Zhao C, J. Mater. Chem. B 2013, 1, 265. [PubMed: 32260750]

[64]. Oh H, Lee J, Lee M, Appl. Surf. Sci. 2018, 427, 65.

[65]. Tittle CM, Yilman D, Pope MA, Backhouse CJ, Adv. Mater. Technol. 2018, 3, 1700207.

[66]. Abdulhafez M, Tomaraei GN, Bedewy M, ACS Appl. Nano Mater. 2021, 4, 2973.

[67]. Yanez-Sedeno P, Pingarron JM, Anal. Bioanal. Chem. 2005, 382, 884. [PubMed: 15864491]

[68]. Oh SY, Hong SY, Jeong YR, Yun J, Park H, Jin SW, Lee G, Oh JH, Lee H, Lee S-S, ACS Appl. Mater. Interfaces 2018, 10, 13729. [PubMed: 29624049]

[69]. Dong Q, Song D, Huang Y, Xu Z, Chapman JH, Willis WS, Li B, Lei Y, Electrochim. Acta 2018, 281, 117.

[70]. Chinnathambi S, Euverink GJW, J. Electroanal. Chem. 2021, 895, 115530.

[71]. Chaisiwamongkhol K, Batchelor-McAuley C, Compton RG, Analyst 2017, 142, 2828. [PubMed: 28702560]

[72]. Lee YS, Son M, Zhbanov A, Jung Y, Jung MH, Eom K, Nam SH, Park J, Yang S, Sensors 2020, 20, 6231. [PubMed: 33142877]

[73]. Erbach M, Freckmann G, Hinzmann R, Kulzer B, Ziegler R, Heinemann L, Schnell O, J. Diabetes Sci. Technol. 2016, 10, 1161. [PubMed: 27044519]

[74]. Campfield LA, Brandon P, Smith FJ, Brain Res. Bull. 1985, 14, 605. [PubMed: 4027699]

[75]. Campfield LA, Smith FJ, Physiol. Rev. 2003, 83, 25. [PubMed: 12506126]

[76]. Huang NM, Lim HN, Chia CH, Yarmo MA, Muhamad MR, Int. J. Nanomedicine 2011, 6, 3443. [PubMed: 22267928]

[77]. Gökaltun A, Kang YBA, Yarmush ML, Usta OB, Asatekin A, Sci. Rep. 2019, 9, 1. [PubMed: 30626917]

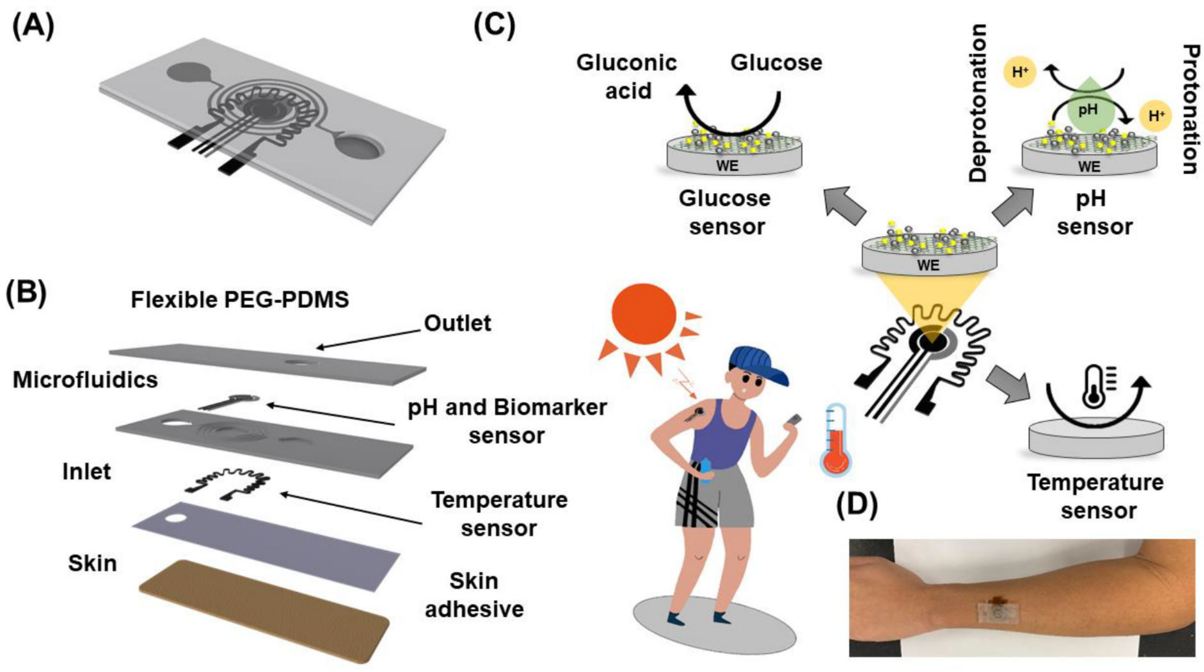

Figure 1. Schematic showing the design, structure, and application of the microfluidic non-enzymatic sweat analysis patch:

(A) Bird's eye and **(B)** exploded views of the patch that integrates dual glucose/pH and temperature sensors with a microfluidic network based on thin PEG-PDMS layers to interface with the skin via a skin-adhesive layer. **(C)** Working principles of functionalized dual glucose/pH and temperature sensors. **(D)** A photograph of the wearable patch on the arm of a human subject.

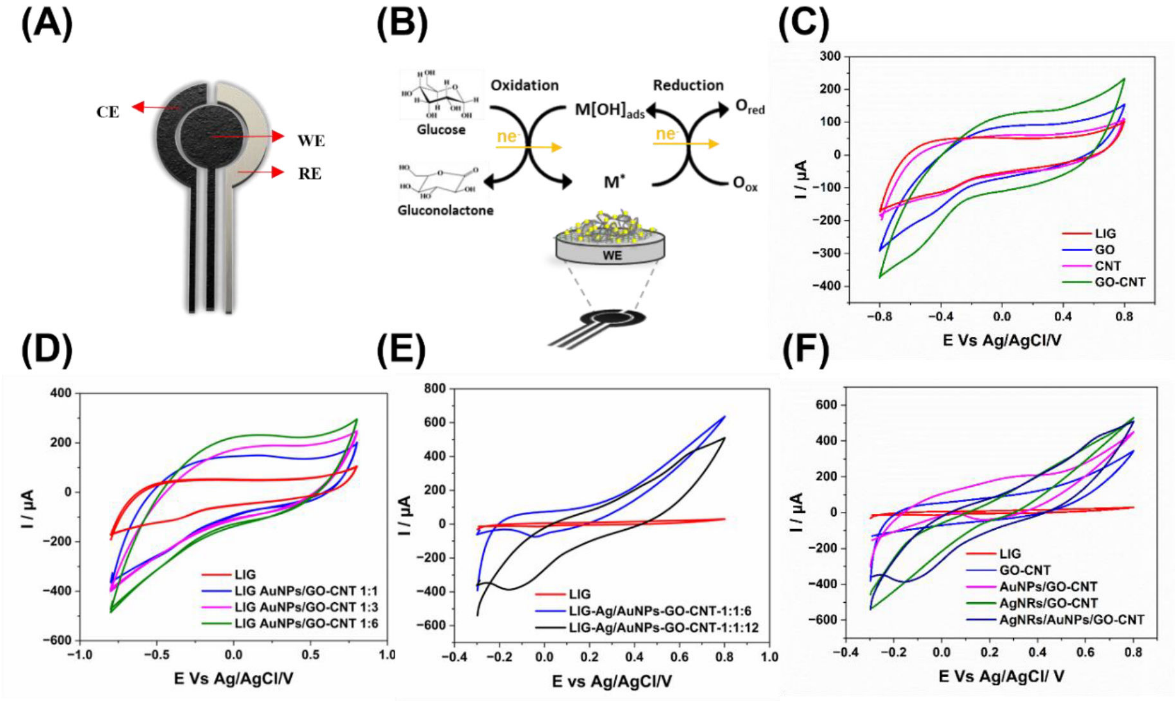

Figure 2. Modification of nanocomposite-LIG electrode glucose sensor before laser treatment. Schematics showing **(A)** the three-electrode electrochemical sensor based on laser-induced graphene (LIG) nanocomposite and **(B)** the electrochemical glucose detection on the LIG working electrode (WE) modified by nanocomposite. **(C)** Performance comparison in cyclic voltammetry curves between the LIG WE with different carbon-based nanomaterial modifications (i.e., LIG, LIG/GO, LIG/CNT, LIG/GO-CNT) for oxidation of glucose. Optimization of the volume ratio of **(D)** gold nanoparticles and **(E)** silver and gold alloys in the GO-CNT matrix. **(F)** Performance comparison in cyclic voltammetry curves between the LIG WE before and after modification with different nanomaterials (i.e., GO-CNT, AuNPs-GO-CNT, AgNRs-GO-CNT, AgNRs/AuNPs-GO-CNT). (Note: 1 mM glucose in 0.1 M NaOH, scan rate 50 mV/s)

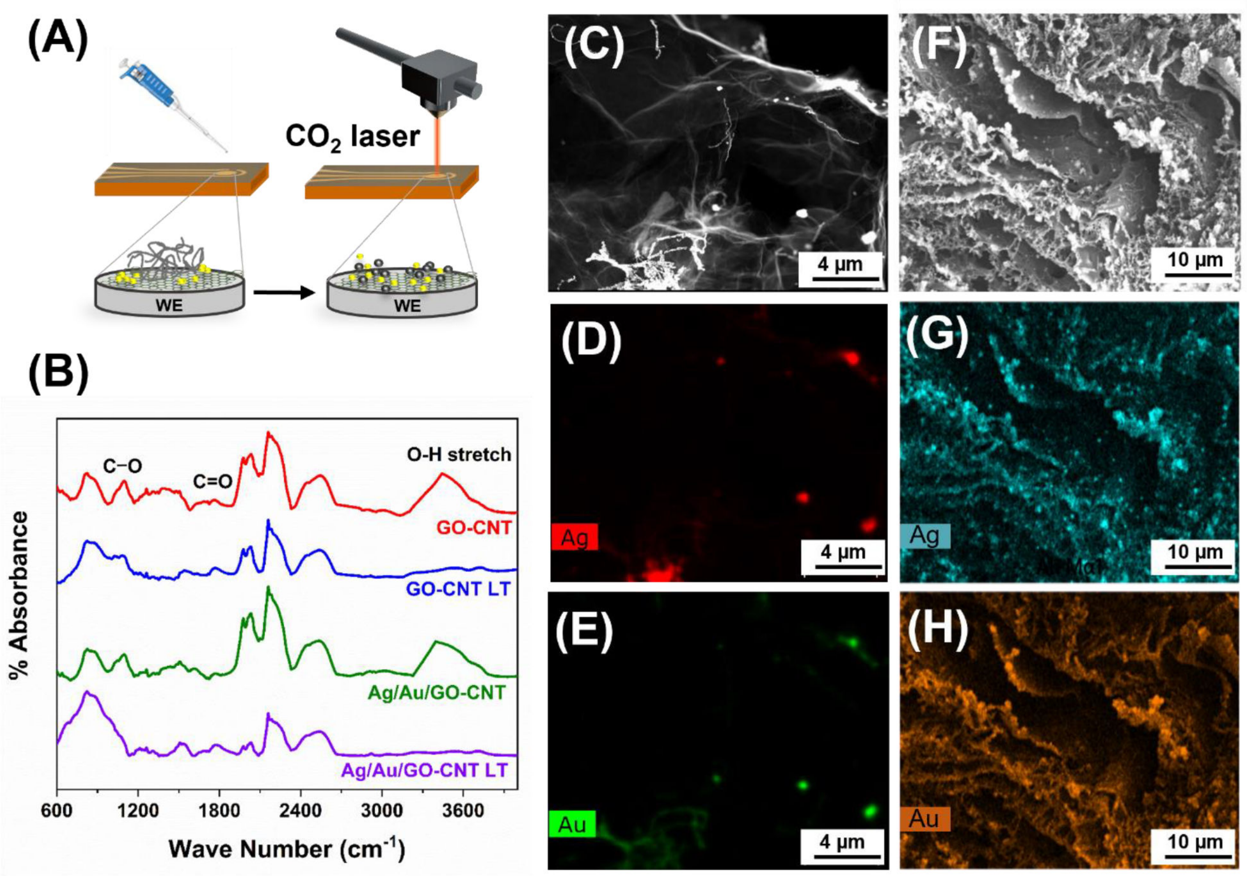

Figure 3. Characterization of laser-treated LIG nanocomposite.

(A) Schematic showing drop-casting of the AgNRs/AuNPs-GO-CNT nanocomposite on the LIG WE (left) and effect of laser treatment to create the Ag/AuNPs-rGO-CNT nanocomposite (right). **(B)** FTIR spectra of the GO-CNT and Ag/AuNPs-rGO-CNT nanocomposite on the LIG WE before and after laser treatment. **(C)** The TEM, and **(D), (E)** EDS mapping images of the Ag/AuNPs-rGO-CNT nanocomposite before laser treatment. **(F)** The FESEM, and **(G)**, **(H)** EDS mapping images of the Ag/AuNPs-rGO-CNT nanocomposite on the LIG WE after laser treatment.

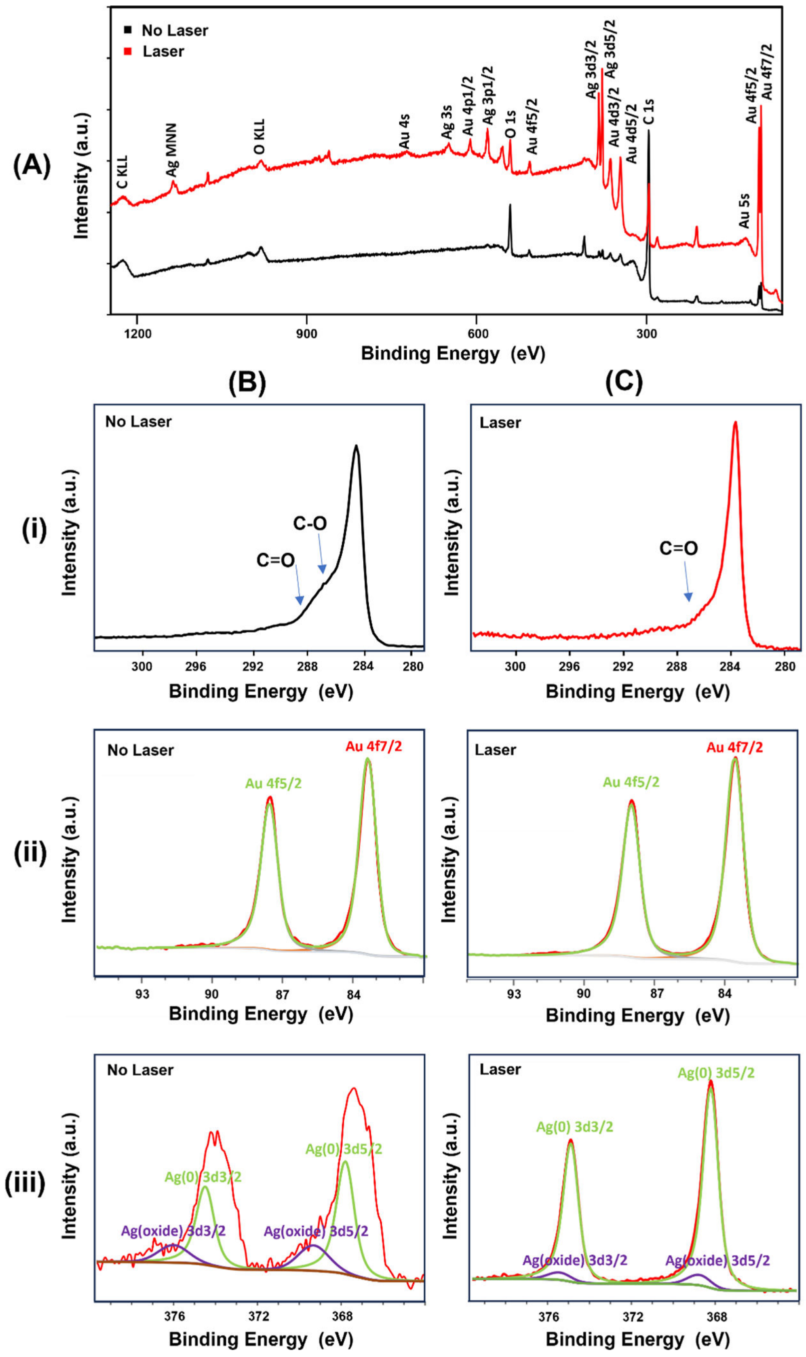

Figure 4. XPS spectra of the AgNRs/AuNPs-GO-CNT nanocomposite.

(A) Survey scan and zoom-in views of the Ag/AuNPs-rGO-CNT nanocomposite **(B)** before and **(C)** after laser treatment in the **(i)** [280, 304], **(ii)** [81, 95], and **(iii)** [364, 380] eV regions.

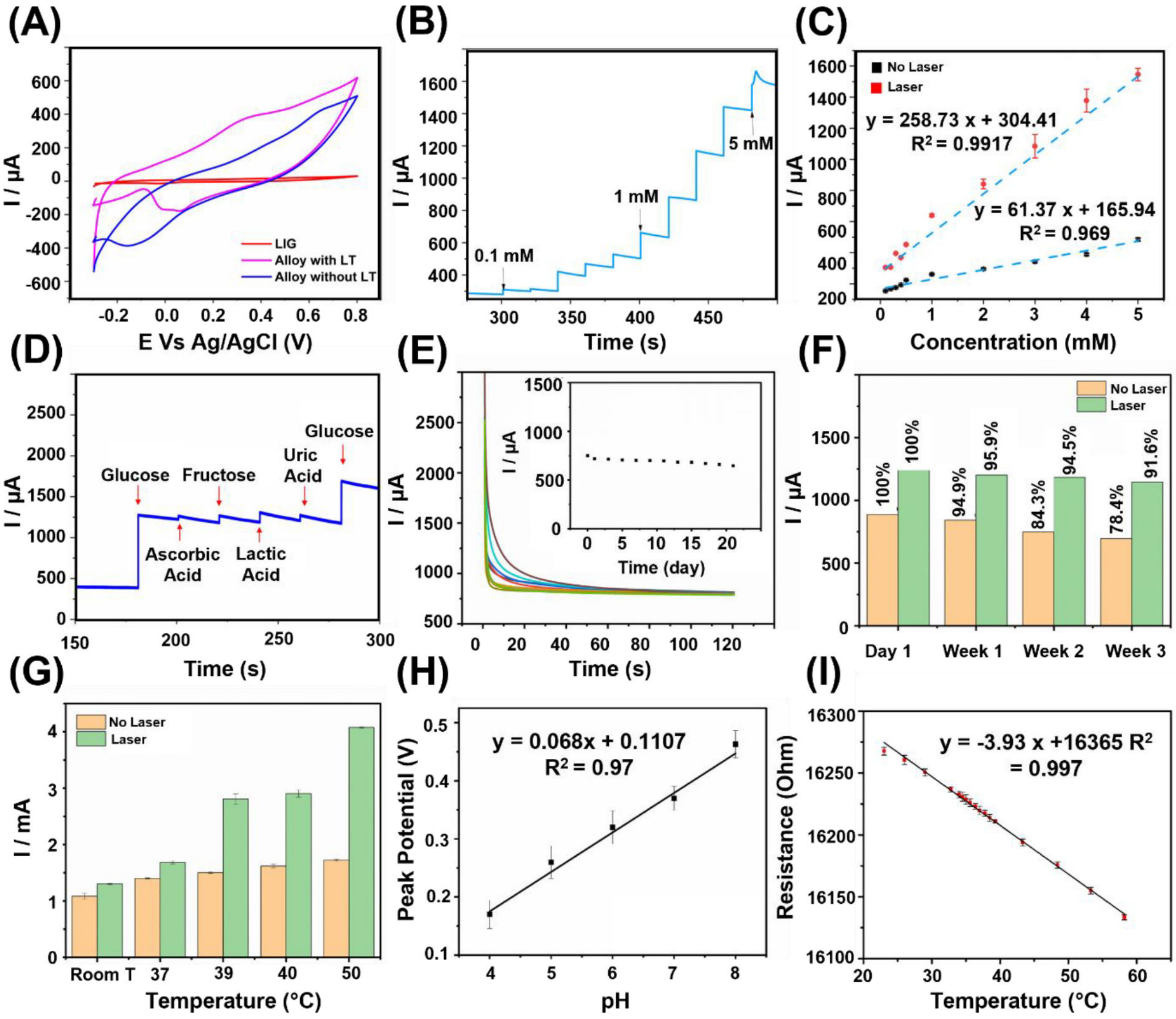

Figure 5. Effect of the laser treatment on the Ag/AuNPs-rGO-CNT nanocomposite-modified biosensors.

(A) Comparison of the CV curves of the Ag/AuNPs-rGO-CNT nanocomposite-modified LIG WE before and after laser treatment (1 mM glucose in 0.1 M NaOH, scan rate 50 mV/s). **(B)** Amperometric response of the laser-treated sensor to increased glucose concentration from consecutive injection into the stirred 0.1 M NaOH (applied potential of +0.7 V vs. Ag/AgCl) and **(C)** the comparison of calibration curve before and after laser treatment. **(D)** Selectivity study of the sensor to 5 mM glucose, 25 µM ascorbic acid, 20 µM fructose, 5 mM lactic acid, and 20 µM uric acid (at +0.7 V). **(E)** The stability of the biosensor was kept in ambient conditions between such successive runs to 1 mM glucose over three weeks, with the corresponding current-time plot of the chronoamperometric response shown in the inset. Comparison in the **(F)** stability of and **(G)** temperature effect on chronoamperometric responses between Ag/AuNPs-rGO-CNT nanocomposite-modified glucose sensors with and without laser treatment in artificial sweat with 1 mM glucose. **(H)** The dependence of the peak potential of the dual-mode sensor on the pH. **(I)** Resistive responses of the LIG-based temperature sensor as a function of temperature in the physiologically relevant range.

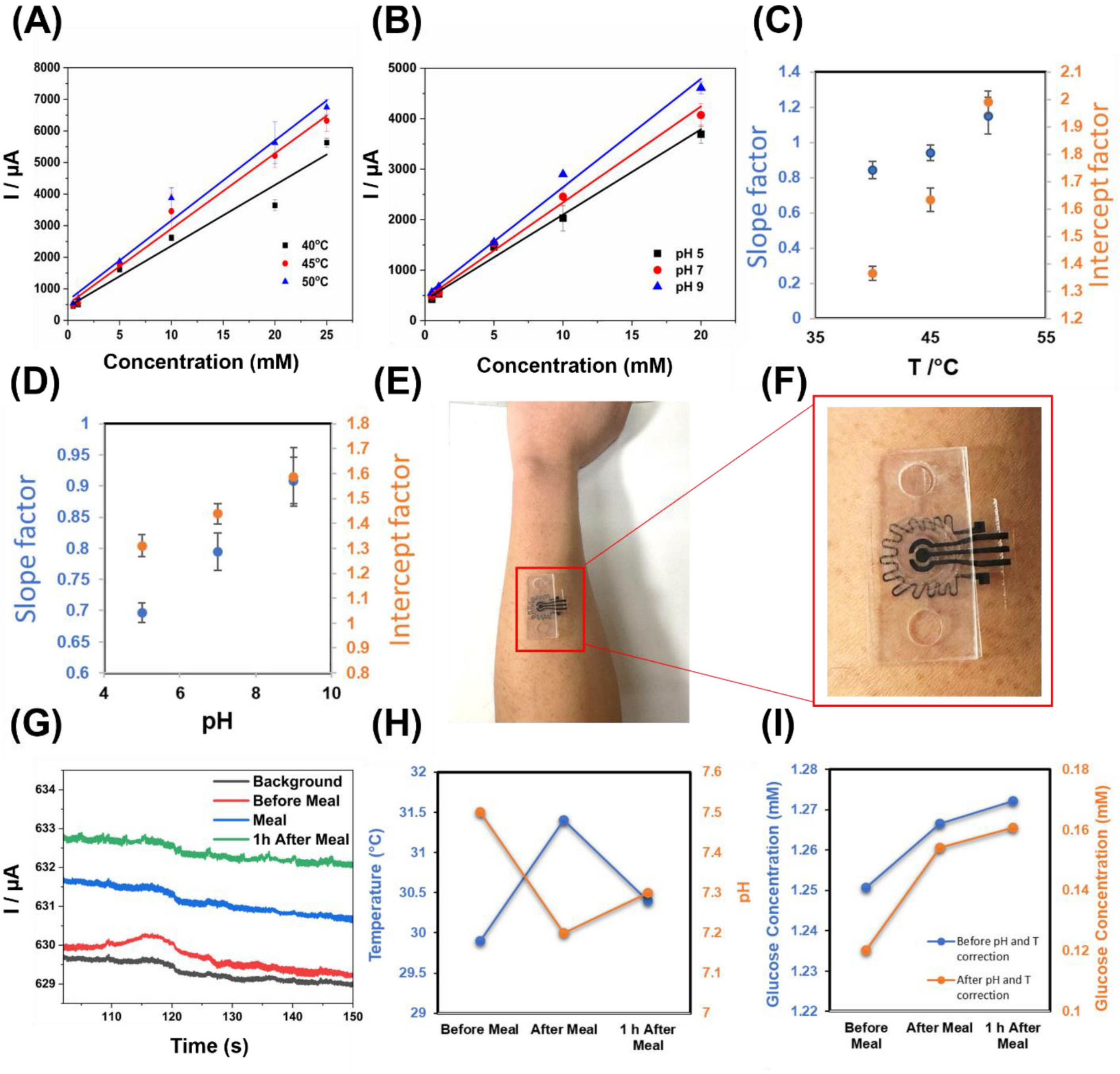

Figure 6. Calibration of the glucose sensor with simultaneously measured pH/temperature and its integration with a microfluidic patch for on-body glucose analysis.

Calibration curves of the glucose sensor at different **(A)** temperatures (40, 45, and 50°C) and **(B)** pH values (5, 7, and 9). Correction factors as a function of sweat **(C)** temperature and **(D)** pH. **(E)** Optical images of the microfluidic sensing patch on the forearm of a human subject, with an enlarged view of the patch shown in **(F)**. **(G)** Chronoamperometric responses of the glucose sensor before, immediately after, and 1 h after the meal, together with **(H)** simultaneously measured pH levels and the skin temperature. **(I)** Comparison of the glucose concentration before and after pH and temperature calibrations.